J. Fluid Mech. (2014), *vol.* 757, *pp.* 33–56.
doi:10.1017/jfm.2014.473

Mixed convection in a horizontal duct with bottom heating and strong transverse magnetic field

Xuan Zhang[1] **and Oleg Zikanov**[1,†]

[1]Department of Mechanical Engineering, University of Michigan – Dearborn, MI 48128-1491, USA

(Received 26 March 2014; revised 11 June 2014; accepted 12 August 2014;
first published online 19 September 2014)

Mixed convection in a horizontal duct with imposed transverse horizontal magnetic field is studied using direct numerical simulations (DNS) and linear stability analysis. The duct's walls are electrically insulated and thermally insulated with the exception of the bottom wall, at which constant-rate heating is applied. The focus of the study is on flows at high Hartmann ($Ha \leqslant 800$) and Grashof ($Gr \leqslant 10^9$) numbers. It is found that, while conventional turbulence is fully suppressed, the natural convection mechanism leads to the development of large-scale coherent structures. Two types of flows are found. One is the 'low-Gr' regime, in which the structures are rolls aligned with the magnetic field and velocity and temperature fields are nearly uniform along the magnetic field lines outside of the boundary layers. Another is the 'high-Gr' regime, in which the convection appears as a combination of similar rolls oriented along the magnetic field lines and streamwise-oriented rolls. In this case, velocity and temperature distributions are anisotropic, but three-dimensional.

Key words: convection, high-Hartmann-number flows, MHD and electrohydrodynamics

1. Introduction

It is known that a sufficiently strong imposed magnetic field can completely change the nature of flows of electrically conducting fluids. The effect is due to the Lorentz force and the conversion of flow's kinetic energy into heat by the Joule dissipation of induced electric currents. The main components of the effect are: (i) suppression of conventional turbulence, (ii) suppression of velocity structures with strong gradients along the magnetic field lines and (iii) formation of flow states with thin and strongly sheared magnetohydrodynamic (MHD) boundary layers. An explanation and extensive discussion of the effect can be found, for example, in Davidson (2001) or Branover (1978).

In this paper, we consider the influence of very strong (high-Hartmann-number) magnetic fields on mixed (combined natural and forced) thermal convection in flows of liquid metals. This combination of physical effects can be found in currently designed liquid metal (likely, Li or PbLi) blankets for future nuclear fusion reactors (see, e.g., the chapter by Bühler in Molokov, Moreau & Moffatt 2007). The key component of a blanket is a network of liquid metal flows in long duct-shaped conduits arranged into a shield around the reaction zone. The flows are subject to

† Email address for correspondence: zikanov@umich.edu

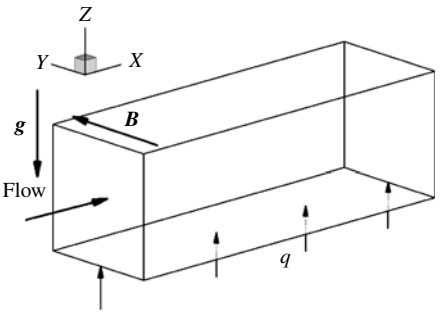

FIGURE 1. Flow geometry and coordinate system. The arrows marked by letters $\boldsymbol{g}$, $\boldsymbol{B}$ and q denote, respectively, the orientations of the gravity acceleration, magnetic field and wall heating.

very strong (up to 10–12 T in a full-scale reactor) steady magnetic fields. They also experience strong heat load concentrated near the wall facing the reactor (see, e.g., Smolentsev, Moreau & Abdou 2008; Smolentsev *et al.* 2010). Since, as shown, e.g., by Zikanov & Thess (1998), Lee & Choi (2001) or Krasnov, Zikanov & Boeck (2012), conventional turbulence is most likely fully suppressed by such a strong magnetic field, the flow structure and the distribution of temperature are largely determined by the buoyancy force in its interaction with the Lorentz force, viscous friction and imposed pressure gradients.

Several attempts of computational analysis of the thermal convection phenomena in configurations corresponding to specific designs of fusion reactor blankets have been performed. Some examples are Tagawa, Authié & Moreau (2002), Authié, Tagawa & Moreau (2003), Mas de les Valls *et al.* (2011), Mistrangelo & Bühler (2013) and Vetcha *et al.* (2013). Such analyses typically face insurmountable obstacles of extremely high requirements on numerical resolution, which have to be satisfied in order to accurately compute flow features, most importantly the MHD boundary layers. The problem is typically resolved in one of the three ways: by running under-resolved simulations, by considering flows at the Hartmann and Grashof numbers, which are several orders of magnitude lower than in the reactor conditions, or, finally, by accepting an approximation, in which the flow is quasi-two-dimensional or steady-state, or both. The quasi-two-dimensional approximation of Sommeria & Moreau (1982), according to which the flow structures are uniform along the magnetic field lines except within the Hartmann boundary layer, is especially relevant in the blanket case and, therefore, widely used.

This paper takes a different approach. We believe that convection in the presence of a strong magnetic field needs to be understood in its basic features before specific blanket designs can be analysed in all their complexity. The approach calls for studies of well-defined simplified systems. One such system analysed in this paper is illustrated in figure 1. We consider a fully developed flow in a long horizontal duct. Constant-rate heating is applied to the bottom wall. A uniform magnetic field oriented in the transverse horizontal direction is imposed in the entire flow domain. No assumptions are made concerning the spatial dimensionality and time dependency of the flow.

The immediate precursor of our work is the paper of Zikanov, Listratov & Sviridov (2013), where the linear stability and direct numerical simulation (DNS) analyses were conducted for the flow through a round horizontal pipe with transverse horizontal

magnetic field and uniform constant-rate heating applied to the bottom half of the wall. The computational work was performed in an attempt to explain the results of the experiments of Genin *et al.* (2011) where temperature fluctuations disappeared at moderately strong magnetic fields clearly indicating suppression of turbulence, but reappeared at stronger magnetic field in the form of high-amplitude low-frequency oscillations. The results of the numerical analysis of Zikanov *et al.* (2013) were in remarkably good quantitative agreement with the experimental data. The analysis confirmed the earlier suggested explanation that the oscillations were caused by the change of the type of the most unstable convection modes. As the strength of the magnetic field increased, the preferential suppression of flow structures having large gradients along the field lines resulted in the most unstable modes taking the form of convection rolls with axes aligned with the field. Transport of the rolls by the mean flow resulted in quasi-periodic fluctuations of temperature.

Our analysis of the duct flow is conducted in a manner similar to that of Zikanov *et al.* (2013). After presenting the computational model in § 2, we discuss the results concerning the streamwise-independent base flow (in § 3) and its linear instability (in § 4). The results of DNS are discussed in § 5. Finally, concluding remarks are given in § 6.

2. Physical model and numerical method

2.1. *Physical model*

The liquid metal is modelled as an incompressible, electrically conducting (but not magnetizable) Newtonian viscous fluid with constant physical properties. The Boussinesq approximation is applied for the temperature-related buoyancy force. Following the assumption of small magnetic Reynolds and Prandtl numbers (typically valid in technological applications including fusion reactor blankets), we use the quasi-static approximation (see, e.g., Branover 1978; Davidson 2001). The component of the magnetic field induced by flow velocity is neglected in comparison with the imposed field in the expressions for the Lorentz force and Ohm's law.

The flow configuration is illustrated in figure 1. The fluid moves through a horizontal duct of square cross-section. Spatially uniform and time-independent magnetic field $\boldsymbol{B} = B\boldsymbol{e}_y$ is imposed in the horizontal transverse direction. The duct walls are electrically perfectly insulating. The top and side walls are also thermally perfectly insulating, while the bottom wall is subject to uniform heating with the heat flux intensity q. We use the wall heating as a model of the volumetric heating by neutrons in actual blankets. This choice is dictated by our desire to avoid the uncertainty associated with the selection of volumetric heating parameters and justified by the fact that the volumetric heating occurs primarily near one wall and subsides exponentially with the distance to this wall (see, e.g., Smolentsev, Morley & Abdou 2006).

A fully developed portion of the flow occurring in a long duct is considered. This is an idealization of the situation in a fusion reactor blanket, where the duct is likely to have the length equal to a few tens of hydraulic diameters. As a justification of our approach, we mention that the majority of the flows discussed in our paper are characterized by large values of Hartmann numbers defined later in this section. This means that the Lorentz force has much larger typical amplitude than the viscous force, and the flow becomes fully developed at a much shorter distance from the inlet than in the non-MHD case.

The governing equations are non-dimensionalized using the duct half-width d as the length scale, mean streamwise velocity U as the velocity scale, wall heating-based

group qd/κ, where κ is the thermal conductivity, as the temperature scale, B as the scale of the magnetic field strength and dUB as the scale of electric potential. The non-dimensional governing equations are

$$\frac{\partial \boldsymbol{u}}{\partial t} + (\boldsymbol{u}\cdot\nabla)\boldsymbol{u} = -\nabla p - \nabla\hat{p} - \nabla\tilde{p} + \frac{1}{Re}\nabla^2\boldsymbol{u} + \boldsymbol{F}_b + \boldsymbol{F}_L, \tag{2.1}$$

$$\nabla\cdot\boldsymbol{u} = 0, \tag{2.2}$$

$$\frac{\partial\theta}{\partial t} + \boldsymbol{u}\cdot\nabla\theta = \frac{1}{Pe}\nabla^2\theta - u_x\frac{\mathrm{d}T_m}{\mathrm{d}x}. \tag{2.3}$$

Here, $\boldsymbol{u}$ is the velocity field. The composition of pressure term is discussed later in this section. The temperature field is a sum

$$T(\boldsymbol{x}, t) = T_m(x) + \theta(\boldsymbol{x}, t) \tag{2.4}$$

of fluctuations θ and the mean mixed temperature

$$T_m(x) = \frac{\displaystyle\int_A u_x T\,\mathrm{d}A}{\displaystyle\int_A u_x\,\mathrm{d}A} = \frac{1}{A}\int_A u_x T\,\mathrm{d}A, \tag{2.5}$$

where A is the cross-section area of the duct. One can also use the decomposition into fluctuations and simple mean temperature $\bar{T}(x) = A^{-1}\int_A T\,\mathrm{d}A$. Applying the energy balance between the wall heating and the streamwise convection heat transfer, we find that $T_m(x)$ and $\bar{T}(x)$ are linear functions with the same derivative:

$$\frac{\mathrm{d}T_m}{\mathrm{d}x} = \frac{\mathrm{d}\bar{T}}{\mathrm{d}x} = \frac{\mathrm{P}}{APe} = \frac{2}{Pe}, \tag{2.6}$$

where P is the perimeter of the heated portion of the wall.

The buoyancy and Lorentz forces are computed as

$$\boldsymbol{F}_b = Gr\,Re^{-2}\boldsymbol{e}_z T, \tag{2.7}$$

$$\boldsymbol{F}_L = Ha^2 Re^{-1}\boldsymbol{j}\times\boldsymbol{e}_y, \tag{2.8}$$

where $\boldsymbol{e}_z$ is the unit vector opposite to the direction of gravity and $\boldsymbol{e}_y$ is the unit vector along the imposed magnetic field. The electric current $\boldsymbol{j}$ is determined by the Ohm's law

$$\boldsymbol{j} = -\nabla\phi + \boldsymbol{u}\times\boldsymbol{e}_y, \tag{2.9}$$

where the electric potential ϕ is a solution of the Poisson equation expressing the instantaneous electric neutrality of the fluid assumed in the quasi-static approximation:

$$\nabla^2\phi = \nabla\cdot(\boldsymbol{u}\times\boldsymbol{e}_y). \tag{2.10}$$

The boundary conditions at the duct walls are the no-slip conditions for velocity

$$\boldsymbol{u} = 0 \quad \text{at } y = \pm 1,\ z = \pm 1, \tag{2.11}$$

perfect electric insulation

$$\frac{\partial\phi}{\partial n} = 0 \quad \text{at } y = \pm 1,\ z = \pm 1, \tag{2.12}$$

and conditions of constant-rate heating at the lower wall and thermal insulation at the other walls

$$\frac{\partial\theta}{\partial z} = -1 \quad \text{at } z = -1, \tag{2.13}$$

$$\frac{\partial\theta}{\partial n} = 0 \quad \text{at } y = \pm 1, z = 1. \tag{2.14}$$

The inlet–exit conditions are, in agreement with our assumption of a fully developed flow, those of periodicity of the velocity $\boldsymbol{u}$, temperature fluctuations θ and pressure fluctuations p.

The non-dimensional parameters are the Reynolds number

$$Re \equiv \frac{Ud}{\nu}, \tag{2.15}$$

the Péclet number

$$Pe \equiv \frac{Ud}{\chi} = Re\,Pr, \tag{2.16}$$

where $Pr = \nu/\chi$ is the Prandtl number, the Hartmann number

$$Ha \equiv Bd\left(\frac{\sigma}{\rho\nu}\right)^{1/2}, \tag{2.17}$$

and the Grashof number

$$Gr \equiv \frac{g\beta q d^4}{\nu^2\kappa}, \tag{2.18}$$

where χ is the temperature diffusivity, σ is the electric conductivity and ν is the kinematic viscosity of the liquid.

We now address the pressure decomposition in (2.1), according to which the total pressure P is

$$P = \hat{p}(x) + \tilde{p}(x, z) + p(\boldsymbol{x}, t). \tag{2.19}$$

Here $\hat{p}$ is a linear function of x corresponding to a spatially uniform streamwise gradient $\mathrm{d}\hat{p}/\mathrm{d}x$. The gradient is routinely used in simulations of fully developed duct, pipe and channel flows as a flow-driving mechanism. In our model, $\mathrm{d}\hat{p}/\mathrm{d}x$ is adjusted at every time step to maintain constant mean velocity. As discussed by Alboussière, Garandet & Moreau (1993), Lyubimova *et al.* (2009) or Zikanov *et al.* (2013), the rest of the decomposition becomes necessary in numerical models of mixed convection in non-vertical channels with periodic inlet–exit conditions. Only the fluctuations p satisfy these conditions. The additional component

$$\tilde{p}(x, z) = \frac{\mathrm{d}T_m}{\mathrm{d}x}\frac{Gr}{Re^2}xz = \frac{\mathrm{P}}{APe}\frac{Gr}{Re^2}xz \tag{2.20}$$

arises due to the buoyancy force

$$\tilde{\boldsymbol{F}}_b = \frac{Gr}{Re^2}T_m(x)\boldsymbol{e}_z \tag{2.21}$$

caused by the mean-mixed temperature T_m. The force increases linearly with x. It has non-zero curl and, thus, cannot be cancelled by a pressure gradient. As one can read in Alboussière *et al.* (1993) or Lyubimova *et al.* (2009) or deduce directly from (2.21), a pressure distribution, vertical gradient of which balances $\tilde{\boldsymbol{F}}_b$, has, up

to an additive constant, the form (2.20). The distribution has non-zero z-dependent streamwise gradient, which drives the flow in the positive x direction in the lower part of the duct and in the negative x direction in its upper part. As already demonstrated by Zikanov *et al.* (2013) and confirmed by the results of this paper, at high Gr, the extra force can lead to a perceptible top–bottom asymmetry of the streamwise velocity profile.

2.2. *Numerical method*

The numerical method is a version of the finite difference model first introduced by Krasnov, Zikanov & Boeck (2011) and later used for various flows at strong magnetic fields (e.g. by Krasnov *et al.* 2012; Zhao & Zikanov 2012; Zikanov *et al.* 2013). The spatial discretization is of the second order and performed on a non-uniform collocated grid. The grid is clustered towards the walls according to the coordinate transformations

$$y=\frac{\tanh(A_y\eta)}{\tanh(A_y)},\quad z=\frac{\tanh(A_z\xi)}{\tanh(A_z)}, \tag{2.22a,b}$$

where $(\eta$–$\xi)$ are the transformed coordinates, in which the grid is uniform, and A_y, A_z are the coefficients determining the degrees of clustering.

An important feature of the spatial discretization is its conservative character. Spatial derivatives are evaluated using the velocity and current fluxes as proposed by Morinishi *et al.* (1998) and Ni *et al.* (2007). The fluxes are obtained by special interpolations to half-integer grid points. This renders the scheme perfectly conservative in the non-viscous non-conductive limit in regards of mass, momentum, electric charge and thermal energy. The conservation of kinetic energy is satisfied with a dissipative error of the third order.

The time discretization uses the standard projection algorithm (see, e.g., Zikanov 2010). The body forces and nonlinear convection terms are treated explicitly using the backward difference Adams–Bashforth scheme as described by Krasnov *et al.* (2011). The conduction and viscosity terms are treated implicitly in order to avoid the stringent stability limitations on the time step that arise at strong near-wall clustering.

The time step from t^n to $t^{n+1}=t^n+\Delta t$ consists of the following substeps.

(i) Solving the Poisson equation for electric potential and computing the body forces:

$$\nabla^2\phi^n=\boldsymbol{\nabla}\cdot(\boldsymbol{u}^n\times\boldsymbol{e}_y), \tag{2.23}$$

$$\boldsymbol{j}^n=-\boldsymbol{\nabla}\phi^n+\boldsymbol{u}^n\times\boldsymbol{e}_y, \tag{2.24}$$

$$\boldsymbol{F}_b^n=Gr\,Re^{-2}\boldsymbol{e}_zT^n, \tag{2.25}$$

$$\boldsymbol{F}_L^n=Ha^2Re^{-1}\boldsymbol{j}^n\times\boldsymbol{e}_y. \tag{2.26}$$

The additional pressure components $\hat{p}^n$ and $\tilde{p}^n$ are also computed at this stage.

(ii) Finding the intermediate velocity field $\boldsymbol{u}^*$ from

$$\frac{3\boldsymbol{u}^*-4\boldsymbol{u}^n+\boldsymbol{u}^{n-1}}{2\Delta t}=2\boldsymbol{F}^n-\boldsymbol{F}^{n-1}+\frac{1}{Re}\nabla^2\boldsymbol{u}^*, \tag{2.27}$$

$$\boldsymbol{u}^*=0\quad\text{at } y=\pm1,\ z=\pm1, \tag{2.28}$$

$$\boldsymbol{F}^n=-\boldsymbol{M}(\boldsymbol{u}^n,\boldsymbol{u}^n)-\boldsymbol{\nabla}\hat{p}^n-\boldsymbol{\nabla}\tilde{p}^n+\boldsymbol{F}_b^n+\boldsymbol{F}_L^n, \tag{2.29}$$

where $\boldsymbol{M}(\boldsymbol{u}^n,\boldsymbol{u}^n)$ is the nonlinear term in divergence form. This substep involves solution of three elliptic equations, one for each component of $\boldsymbol{u}^*$.

(iii) Solving the Poisson equation for pressure fluctuations and updating the velocity:

$$\nabla^2 p^{n+1} = \frac{3}{2\Delta t}\nabla \cdot \boldsymbol{u}^*, \tag{2.30}$$

$$\frac{\partial p^{n+1}}{\partial n} = 0 \quad \text{at } y = \pm 1,\ z = \pm 1, \tag{2.31}$$

$$\boldsymbol{u}^{n+1} = \boldsymbol{u}^* - \tfrac{2}{3}\Delta t \nabla p^{n+1}. \tag{2.32}$$

(iv) Solving the implicit equation for temperature:

$$\frac{3\theta^{n+1} - 4\theta^n + \theta^{n-1}}{2\Delta t} = 2G^n - G^{n-1} + \frac{1}{Pe}\nabla^2 \theta^{n+1}, \tag{2.33}$$

where $G^n = -\nabla \cdot (\theta^n \boldsymbol{u}^n) - u_x^n \, \mathrm{d}T_m/\mathrm{d}x$, with the boundary conditions (2.13) and (2.14).

The elliptic equations for potential, pressure, velocity components and temperature are solved using the Fourier decomposition in the streamwise coordinate and the direct reduction solution of the two-dimensional equations for Fourier components conducted on the transformed grid (η–ξ) (see Krasnov *et al.* 2011).

The algorithm is parallelized using the hybrid MPI–OpenMP approach. The MPI memory distribution is along the y-coordinate in the physical space and along the streamwise wavenumber in the Fourier space.

2.3. *Ranges of parameters covered in the numerical analysis*

Single values $Pr = 0.0321$ and $Re = 5000$ are used in the analysis. The first of them corresponds to the LiPb eutectic alloy at temperature around 570 K (Mas de les Valls *et al.* 2008), while the second is selected arbitrarily. In actual liquid metal blankets, the value of Re varies strongly depending on the design. Studying its effect on convection is left for future studies. The Grashof number Gr varies in the range between 10^5 and 10^9. For the Hartmann number we select the range $50 \leqslant Ha \leqslant 800$. As will be seen from our discussion, the upper limit of this range is probably high enough to qualitatively represent the asymptotic flow behaviour at $Ha \sim 10^4$ typical for the liquid metal blankets of fusion reactors.

2.4. *Computational grid*

Accurate numerical simulations of MHD duct flow require sufficient resolution of the Hartmann and Shercliff boundary layers. As demonstrated in the pipe flow analysis of Zikanov *et al.* (2013), good resolution of these layers is necessary for accurate representation of convection structures in the mixed convection case. Considering that the non-dimensional thicknesses of the boundary layers scale, respectively, as Ha^{-1} and $Ha^{-1/2}$, resolving them becomes a challenging task in flows with high Ha. In order to assure that the accuracy is achieved in our computations, a grid sensitivity study has been conducted using the base flow with imposed streamwise uniformity (see § 3). As an illustration, the results obtained at $Ha = 300$, $Gr = 10^9$ are presented in table 1. We compare the computed values of the integrated friction forces at the Hartmann and Shercliff walls of the duct:

$$\tau_{Ha} = \tau_y = \frac{1}{Re}\sum_{y\pm 1}\int_{-1}^{1}\frac{\partial u_x}{\partial y}\,\mathrm{d}z, \tag{2.34}$$

$$\tau_{Sh} = \tau_z = \frac{1}{Re}\sum_{z\pm 1}\int_{-1}^{1}\frac{\partial u_x}{\partial z}\,\mathrm{d}y. \tag{2.35}$$

N_y	N_z	A_y	A_z	$-\tau_{Ha}$	$-\tau_{Sh}$	ϵ	N_{Ha}	N_{Sh}
64	64	3.0	2.0	0.0582	0.0075	0.0013	3	8
96	96	2.0	2.0	0.0515	0.0076	0.0139	2	12
96	96	3.0	2.0	0.0585	0.0075	0.0006	5	12
96	96	3.5	2.0	0.0587	0.0075	0.0001	8	12
128	96	3.0	2.0	0.0585	0.0075	0.0004	6	12
128	128	3.0	2.0	0.0586	0.0075	0.0003	6	16

TABLE 1. An example of grid sensitivity study conducted, here, for $Ha = 300$ and $Gr = 10^9$. Here τ_{Ha} and τ_{Ha} are the wall friction forces (2.34) and (2.35),ϵ is the absolute error of the balance (2.36) and N_{Ha} and N_{Sh} are the numbers of grid points within, accordingly, Hartmann and sidewall (Shercliff) boundary layers.

Ha	Gr	N_y	N_z	A_y	A_z	N_x (stability analysis)	L_x (DNS)	N_x (DNS)
50	All	64	64	2.5	2.0	32	4π	128
100	All	96	96	3.0	2.0	32	4π	128
200	10^6, 10^7, 10^8	96	96	3.5	2.0	32	4π	128
200	10^9	96	96	3.5	2.0	32 or 64	2π	128
300	10^6, 10^7	96	96	3.5	2.0	32	4π	128
300	10^8	128	96	3.0	2.0	32 or 64	4π	256
300	10^9	128	96	3.0	2.0	32 or 64	2π	256
400	10^6, 10^7	96	96	3.5	2.0	32	4π	128
400	10^8	128	96	3.0	2.0	32 or 64	4π	256
400	10^9	128	96	3.0	2.0	32 or 64	2π	256
800	10^6	128	96	4.0	3.0	32	4π	128
800	10^7	128	96	4.0	3.0	32	4π	256
800	10^8	128	96	4.0	3.5	32 or 64	4π	256
800	10^9	128	96	4.0	3.5	32 or 64	4π	256

TABLE 2. Parameters of the computational grids used in simulations.

In a fully developed steady-state flow, the integrated Lorentz and buoyancy forces are zero. The wall frictions should be balanced by the driving pressure gradient according to

$$\frac{\mathrm{d}\hat{p}}{\mathrm{d}x} = A^{-1}\left(\tau_{Ha} + \tau_{Sh}\right). \tag{2.36}$$

The error ϵ, with which the computed values satisfy this relation is also used as a measure of the accuracy of the computational model.

In the result of the analysis, the grid with $N_y \times N_z = 128 \times 96$, $A_y = 3.0$ and $A_z = 2.0$ is selected as the one to be used in further computations at $Ha = 300$ and $Gr = 10^9$. This grid has 6 points within each Hartmann layer and 12 points within each Shercliff layer. The maximum and minimum grid steps are $\Delta y_{min} \approx 0.0005$, $\Delta y_{max} \approx 0.047$, $\Delta z_{min} \approx 0.0032$, $\Delta z_{max} \approx 0.043$.

In the just described way, the parameters of the crudest grids providing accurate results have been determined for all of the explored combinations of Ha and Gr. It has been found that the value of Gr does not affect the selection at $Ha \leqslant 200$. At higher Ha, the highest values of Gr require finer resolution. The summary of the grids used in the simulations is presented in table 2.

For the linear stability analysis (§ 4) and three-dimensional DNS (§ 5), we also need to determine the length of computational domain L_x and the number of grid points N_x

in the streamwise direction. The values used in the computations are listed in table 2. For the stability analysis, the domain length is equal to the streamwise wavelength of the tested Fourier mode (see § 4), while N_x is determined in the grid sensitivity study, where we compare the instability growth rates. It has been found that N_x sufficient for accurate computations is independent of the value of Ha. Here $N_x = 32$ is always sufficient at $Gr \leqslant 10^7$. At higher Gr, $N_x = 32$ can be used for modes with short wavelength, approximately smaller than 1.0. Increase to $N_x = 64$ has been found to be necessary for larger wavelengths.

In DNS, computational domains of length $L_x = 4\pi$ or 2π are used. As we will see from the following discussion, the length is more than ten times larger than the streamwise wavelength of the fastest growing instability mode in the interesting cases of large Ha and Gr. The grid step Δx is approximately 0.1 at small Ha or Gr. We have found that at large values of any of these parameters, accurate resolution of velocity and temperature structures near the bottom requires a decrease of Δx to 0.05 or even 0.025.

The maximum time step providing a numerically stable solution is used in the simulations. Its value varies with Ha and Gr, but never exceeds 10^{-2}.

3. Base flow

The base flow, linear stability of which we will study in the next section, is a steady streamwise-uniform flow $\boldsymbol{u}(y, z)$, $\theta(y, z)$, $p(y, z)$. Such two-dimensional solutions always exist and can be computed by artificially imposing uniformity along x, more specifically by applying x-averaging after every time step. To justify our approach, we note that a superposition of the streamwise flow $u_x(y, z)$ and one or several streamwise-uniform convection rolls $(u_y(y, z), u_z(y, z))$ is a natural structure of a laminar flow in our geometry. The analysis of mixed convection in horizontal pipe flow by Zikanov *et al.* (2013) indicates that, even at high Gr, this structure can be stabilized by a moderately strong magnetic field, while a stronger magnetic field can lead to three-dimensional instability and the emergence of another laminar flow regime.

Each solution is computed for sufficiently long time until a fully developed state is reached. Long evolution, sometimes longer than 1000 time units, is typically needed to arrive to this state. The state is unsteady with chaotic behaviour at $Ha = 50$, $Gr \geqslant 10^7$ and at $Ha = 100$, $Gr \geqslant 10^8$. In the more interesting cases of high Ha, the final state of the flow is always steady. The unsteady solutions are ignored in the rest of the paper. The discussion is focused on the steady states and their stability.

The results are presented in figures 2 and 3 and table 3. In addition to visualizations of flow fields in the transverse plane, we use integral quantities, such as the total wall friction force $\mathrm{d}\hat{p}/\mathrm{d}x$, the kinetic energies of streamwise and transverse velocity components

$$E_x = A^{-1} \int_{-1}^{1} \int_{-1}^{1} u_x^2 \,\mathrm{d}y\mathrm{d}z \tag{3.1}$$

$$E_t = A^{-1} \int_{-1}^{1} \int_{-1}^{1} (u_y^2 + u_z^2) \,\mathrm{d}y\mathrm{d}z, \tag{3.2}$$

and the mean square of temperature perturbations

$$E_\theta = A^{-1} \int_{-1}^{1} \int_{-1}^{1} \theta^2 \,\mathrm{d}y\mathrm{d}z. \tag{3.3}$$

Table 3 also shows the maximum and minimum values of u_x.

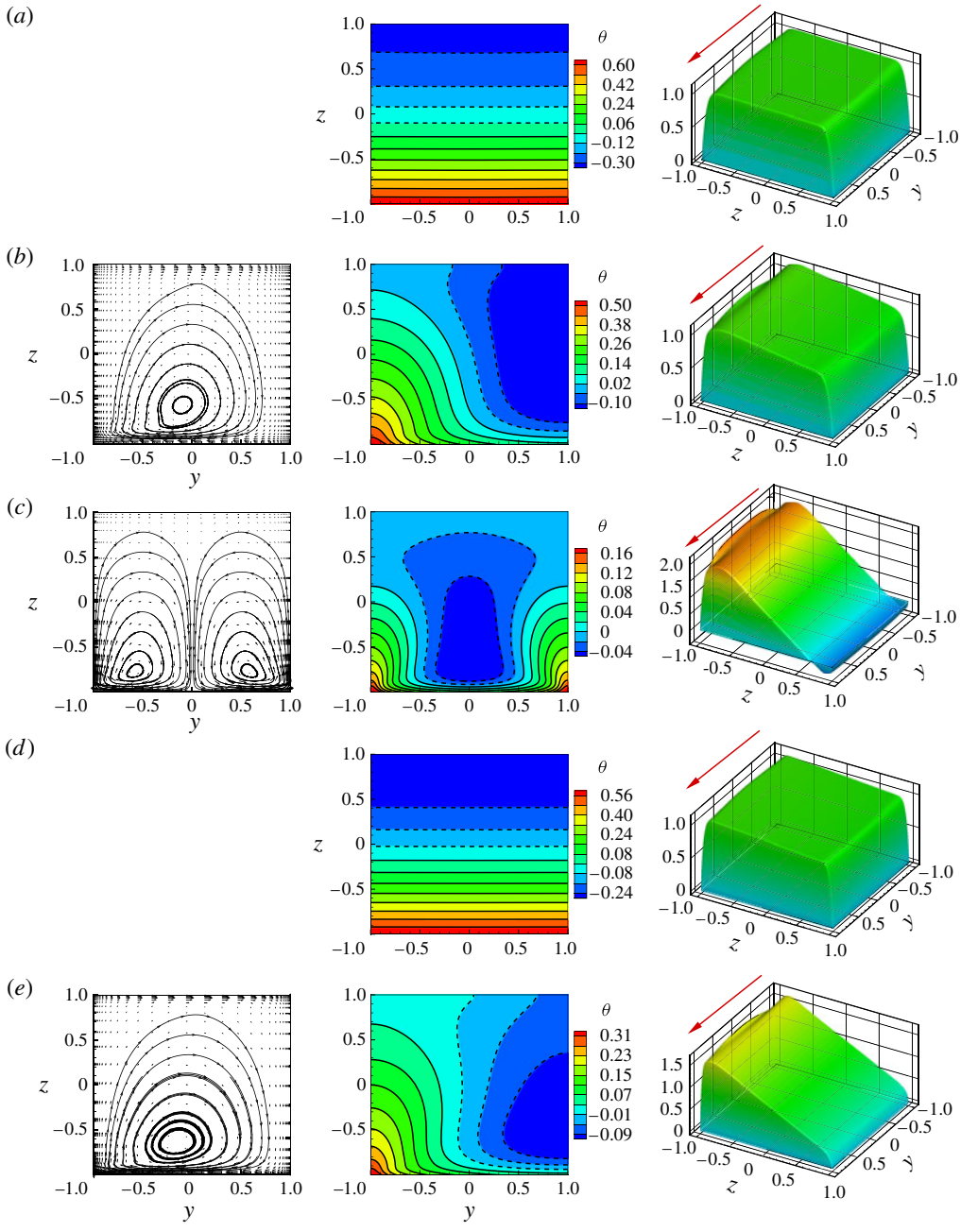

FIGURE 2. (Colour online) Base flow at $Ha = 400$, $Gr = 10^7$ (*a*), $Ha = 400$, $Gr = 10^8$ (*b*), $Ha = 400$, $Gr = 10^9$ (*c*), $Ha = 800$, $Gr = 10^8$ (*d*) and $Ha = 800$, $Gr = 10^9$ (*e*). Vector fields and streamlines of transverse circulation (u_y, u_z) are shown in the left column (not in (*a*) and (*d*), since in these cases the velocity's amplitude is virtually zero). The middle and right columns show distributions of, respectively, temperature fluctuations θ and streamwise velocity u_x. Solid and dashed isolines in the middle column indicate, respectively, positive and negative values. The wall heating is at $z = -1$, and the magnetic field is in the y direction (see the arrows in the right column).

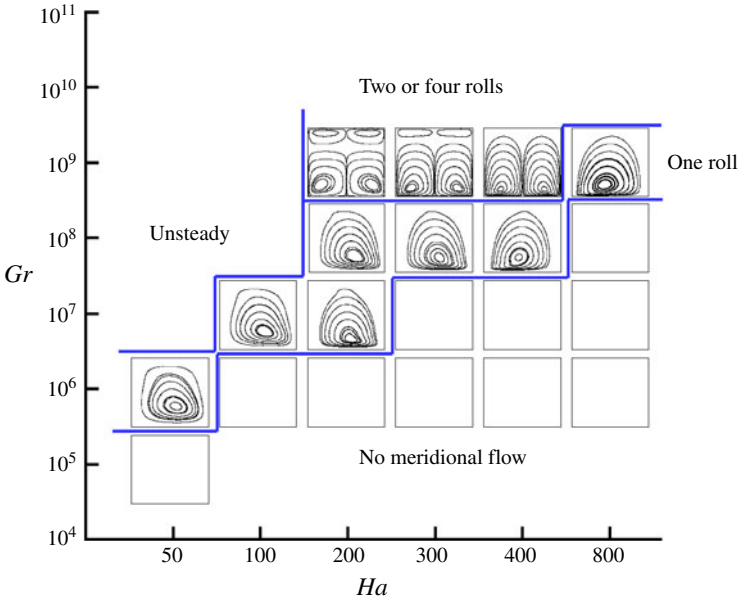

FIGURE 3. (Colour online) Transverse plane circulation patterns found in computed base flows. Blank squares indicate flow regimes, in which the kinetic energy of transverse velocity components E_t (see (3.2)) is less than 10^{-6}.

Ha	Gr	Gr/Ha^2	$-\mathrm{d}\hat{p}/\mathrm{d}x$	E_t	E_θ	E_x	$u_{x,min}$	$u_{x,max}$
50	10^5	4.00×10^1	0.0117	4.00×10^{-10}	9.07×10^{-3}	1.07	0.0	1.161
50	10^6	4.00×10^2	0.0118	2.49×10^{-4}	4.10×10^{-2}	1.06	0.0	1.155
50	10^7	4.00×10^3	0.0126	4.58×10^{-3}	9.77×10^{-3}	1.05	0.0	1.146
100	10^6	1.00×10^2	0.0222	1.42×10^{-9}	8.98×10^{-2}	1.05	0.0	1.107
100	10^7	1.00×10^3	0.0225	1.04×10^{-3}	1.56×10^{-2}	1.04	0.0	1.119
100	10^8	1.00×10^4	0.0236	1.40×10^{-2}	4.12×10^{-3}	1.06	0.0	1.294
200	10^6	2.50×10^1	0.0434	3.80×10^{-11}	8.95×10^{-2}	1.03	0.0	1.070
200	10^7	2.50×10^2	0.0430	1.90×10^{-4}	5.70×10^{-2}	1.03	0.0	1.095
200	10^8	2.50×10^3	0.0433	3.12×10^{-3}	5.82×10^{-3}	1.05	0.0	1.248
200	10^9	2.50×10^4	0.0466	9.05×10^{-3}	1.51×10^{-2}	3.02	−1.388	3.083
300	10^7	1.11×10^2	0.0635	6.90×10^{-10}	8.83×10^{-2}	1.03	0.0	1.070
300	10^8	1.11×10^3	0.0638	1.63×10^{-3}	1.25×10^{-2}	1.04	0.0	1.179
300	10^9	1.11×10^4	0.0664	6.19×10^{-3}	1.18×10^{-3}	2.00	−0.670	2.463
400	10^7	6.25×10^1	0.0841	1.54×10^{-10}	8.85×10^{-2}	1.02	0.0	1.059
400	10^8	6.25×10^2	0.0845	9.60×10^{-4}	2.23×10^{-2}	1.03	0.0	1.157
400	10^9	6.25×10^3	0.0863	4.18×10^{-3}	1.59×10^{-3}	1.61	−0.291	2.109
800	10^6	1.56×10^0	0.1656	2.98×10^{-11}	8.91×10^{-2}	1.02	0.0	1.033
800	10^7	1.56×10^1	0.1656	2.92×10^{-9}	8.70×10^{-2}	1.02	0.0	1.039
800	10^8	1.56×10^2	0.1657	4.95×10^{-8}	8.06×10^{-2}	1.02	0.0	1.099
800	10^9	1.56×10^3	0.1661	2.81×10^{-3}	6.90×10^{-3}	1.19	0.0	1.651

TABLE 3. Integral characteristics of the computed base flow states.

The expected structure of the flow is a combination of streamwise motion and the circulation in the transverse (y–z) plane caused by the convection effect. Figure 2 illustrates the typical laminar flow states on the example of the flows obtained at $Ha = 400$ and $Ha = 800$. At $Ha = 400$, $Gr = 10^7$ and $Ha = 800$, $Gr = 10^8$, the strong magnetic field entirely suppresses transverse circulation. According to table 3, the kinetic energy of this circulation is of the order of 10^{-10} and 10^{-8}, respectively. The profiles of the streamwise velocity are similar to the profiles an isothermal MHD flow would have in the same duct. We see Hartmann and Shercliff boundary layers and nearly flat profiles of core flow. The only visible effect of convection is the slight asymmetry with u_x larger in the bottom (near $z = -1$) than in the top half. This asymmetry is produced by the pressure force $\boldsymbol{\nabla}\tilde{p}$ (see (2.20)) arising in response to the streamwise-non-uniform buoyancy force $\tilde{\boldsymbol{F}}$ associated with the mean-mixed temperature T_m (see Alboussière *et al.* 1993; Lyubimova *et al.* 2009; Zikanov *et al.* 2013). The distribution of temperature fluctuations is nearly one-dimensional $\theta \approx \theta(z)$. In the absence of transverse circulation, the distribution is determined by the balance between conduction and convection by u_x.

When Gr is increased to 10^8 at $Ha = 400$ or to 10^9 at $Ha = 800$, the strength of the magnetic field becomes insufficient to suppress convection circulation. As illustrated in figure 2(*b*,*e*) the circulation takes the form of a single roll. The roll has no preferred circulation direction and may appear in the solution either as shown in the figures or as a symmetric reflection with respect to the vertical midplane. Its kinetic energy is of the order of 10^{-3} in both cases. The circulation affects temperature distribution, which becomes fully two-dimensional and, as a result of mixing, decreases in variation (see values of E_θ in table 3). The shape of streamwise velocity profile does not show a visible effect of the circulation. At the same time, the effect of $\boldsymbol{\nabla}\tilde{p}$ is significant. In both cases, we see strong top–bottom asymmetries. A rudimentary overspeed jet appears near the bottom wall.

Increase of Gr to 10^9 at $Ha = 400$ (see figure 2*c*) changes the structure of the transverse circulation, which takes the form of two symmetric rolls. The kinetic energy of the circulation increases to approximately 4×10^{-3}. Corresponding change of spatial structure and further reduction of variation are observed for the temperature fluctuation field (see figure 2*c* and table 3). The profile of u_x becomes strongly affected by $\boldsymbol{\nabla}\tilde{p}$. We see in figure 2(*c*) and table 3 (note the minimum and maximum values of u_x) that the top–bottom asymmetry evolves to the degree of formation of reverse flow near the top wall.

The summary of the transverse circulation structures of all computed base flows is given in figure 3. Together with the information in table 3, it allows us to see how the tendencies we have just discussed on the example of flow at $Ha = 400$ change with the strength of the magnetic field. At each value of Ha, the Grashof number has to increase above a certain limit to overcome the suppression by the magnetic field and to cause development of convection rolls with non-negligible kinetic energy. The limit increases rapidly with growth of Ha.

As quantified in table 3, growth of Gr at a given Ha leads to a stronger top–bottom asymmetry of the u_x profile and to the appearance of reverse flow near the top wall. Considering the values of E_x, $u_{x,min}$ and $u_{x,max}$, one sees that the effect is weaker at higher Ha.

An important feature to consider is the effect of Gr and Ha on distribution of temperature, in particular, on strength and localization of unstable stratification. One aspect is the influence of transverse circulation that becomes stronger at higher Gr or lower Ha. The circulation leads to stronger mixing, reduction in the overall strength of

unstable stratification, and localization of the strong stratification zone near the heated bottom wall. The top–bottom asymmetry of the streamwise velocity profile, which also grows with Gr and decreases with Ha, has a similar effect. When combined with the linear downstream growth of the mean-mixed temperature (see (2.6)), the streamwise velocity provides asymmetric transport of internal energy, which enhances the unstable stratification in the lower part of the duct, between the wall $z=-1$ and the point where $u_x = u_{x,max}$. Above this point, the stratification is reduced and can even be inverted into a stable one in flows with strong asymmetry and reversed flows (this is registered in our computations at $Ha = 200$ and $Gr = 10^9$). An illustration of the unstable stratification strongly limited to the lower part of the duct is provided by the plot of $\theta(y, z)$ at $Ha = 400$ and $Gr = 10^9$ in figure 2.

4. Linear stability analysis

The linear stability analysis is conducted using a modified version of the numerical model described in § 2.1. We compute the evolution of a solution consisting of the base flow $\boldsymbol{u}_b$, θ_b and the small-amplitude perturbations $\boldsymbol{u}'$, θ'. The perturbations are initially random fields of the average amplitude $\sim 10^{-6}$. During the evolution, the perturbations are constrained to a single Fourier mode of streamwise wavelength λ. This is achieved by applying, after every time step, the filtering operation consisting of fast Fourier transform in x, zeroing out all of the coefficients but the coefficients of the streamwise-uniform (zero) mode and the mode of the wavelength λ, and transforming back into the physical space. The procedure is legitimate as far as the amplitude of the perturbations remains small enough for the quadratic terms in $\boldsymbol{u}'$ and θ' to be negligibly small. The computations are conducted in the domain of length λ with the grid equivalent to the grid used for the base flow in the y and z directions and consisting of 32 or 64 uniformly positioned points in the x direction (see § 2.4 for a discussion of accuracy).

The procedure allows us to determine whether the base flow is linearly unstable to perturbations of the wavelength λ. In the case of instability, the growth rate of perturbations can be determined as

$$\gamma = \frac{1}{2E'}\frac{\mathrm{d}E'}{\mathrm{d}t}, \tag{4.1}$$

where $E' = \langle f'^2 \rangle$, $\langle \cdots \rangle$ stands for volume averaging and f stands for perturbations of a velocity component or temperature. As illustrated in figure 4, in the case of instability, we find a sufficiently long stage of exponential growth, during which all four coefficients γ are nearly constant and equal to each other. The resulting value can be accurately computed to its second digit and is taken as the rate of exponential growth of the instability. We note that in all of the cases, the instability has oscillating nature. The point signals of velocity and temperature oscillate with a nearly constant period and amplitude growing exponentially with time (see the inset of figure 4*a*).

The results are summarized in table 4 and figure 5. The computed values of the exponential growth rate γ and the wavelength λ of the most dangerous mode are shown for the combinations of Ha and Gr, for which the base states are laminar and the stability analysis is conducted. We see in table 4 that the base state is stable at $Ha = 100$ and $Gr = 10^7$, but unstable in all of the other cases. This is consistent with the experimental and computational results obtained by Genin *et al.* (2011) and Zikanov *et al.* (2013) for pipe flows, where at $Gr = 8.5 \times 10^7$ the base flow is stable at $Ha = 100$ and unstable at $Ha = 300$ and 500.

The nature of the instability is illustrated in figure 6. The exponentially growing perturbations have the spatial structure of convection rolls with axes along the

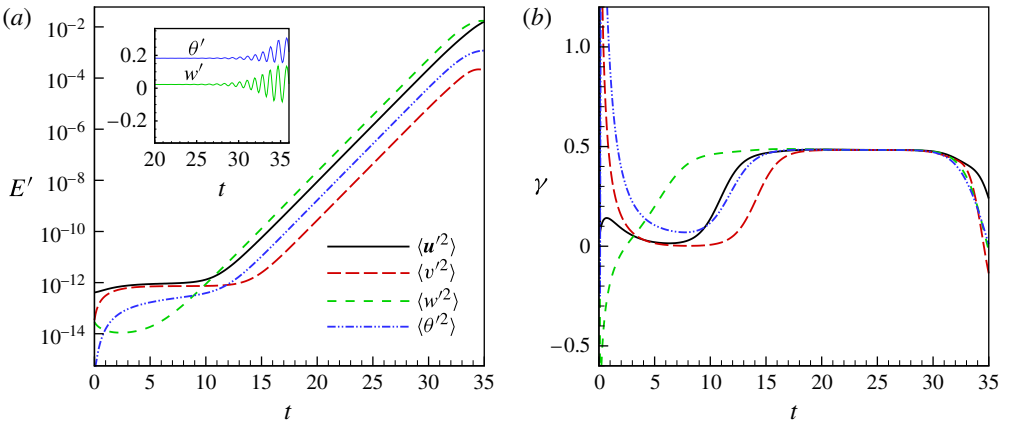

FIGURE 4. (Colour online) Example of linear instability. Perturbation energy E' (a) and coefficient γ (4.1) (b) are shown for $Ha = 400$ and $Gr = 10^8$. Point signals of vertical velocity and temperature perturbations are shown in the inset of (a).

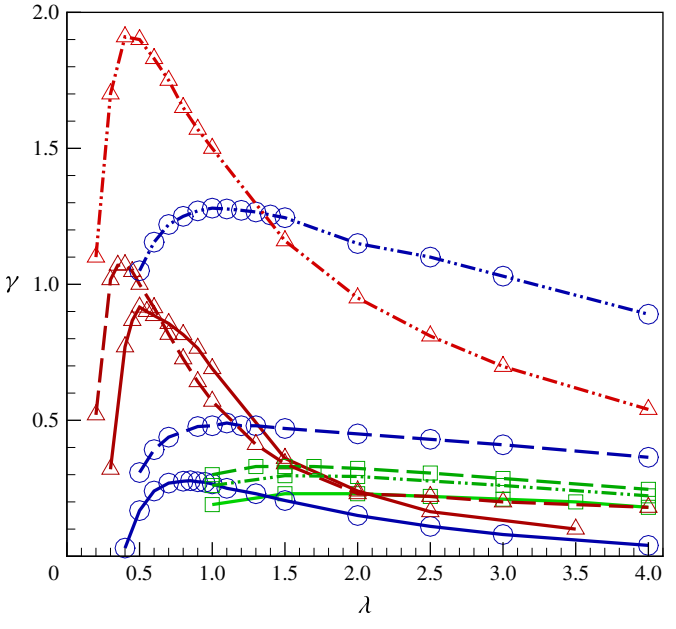

FIGURE 5. (Colour online) Rates of exponential growth shown as functions of axial wavelength λ for $Ha = 200$, $Ha = 400$ and $Ha = 800$ (solid, long-dashed, dash-dot-dot curves) and for $Gr = 10^7$ (squares, green online), $Gr = 10^8$ (circles, blue online), and $Gr = 10^9$ (triangles, red online).

magnetic field lines. The alignment is caused by the selective suppression of the velocity gradients in the field direction by the Joule dissipation. Transport of the rolls by mean flow causes the oscillations of velocity and temperature illustrated in the inset of figure 4(a). To further illustrate the effect we have computed the phase velocity

$$c \equiv \lambda/\Pi, \tag{4.2}$$

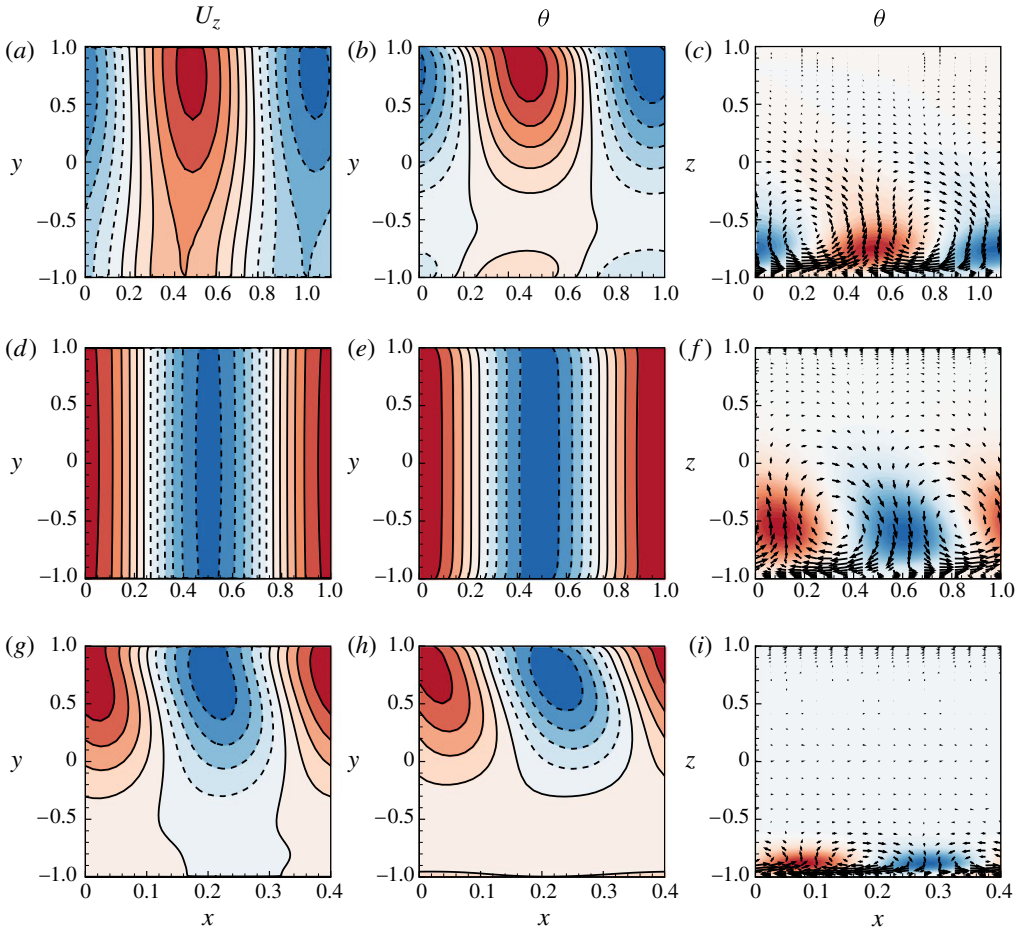

FIGURE 6. (Colour online) Spatial structure of instability modes recorded during the stage of exponential growth at $Ha = 400$, $Gr = 10^8$ (*a*)–(*c*), $Ha = 800$, $Gr = 10^8$ (*d*)–(*f*) and $Ha = 800$, $Gr = 10^9$ (*g*)–(*i*). Perturbations of vertical velocity and temperature at the horizontal midplane section of the duct are shown, respectively, in (*a*), (*d*), (*g*) and (*b*), (*e*), (*h*). Solid and dashed isolines in the left and middle columns indicate, respectively, positive and negative values. Perturbations of temperature and vector fields of velocity perturbations (u', w') are shown in (*c*), (*f*), (*i*).

Ha	100	100	200	200	200	200	300	300	300	400	400	400	800	800	800
Gr	10^6	10^7	10^6	10^7	10^8	10^9	10^7	10^8	10^9	10^7	10^8	10^9	10^7	10^8	10^9
λ	2.0	Stable	2.0	2.0	0.85	0.5	2.0	1.0	0.4	1.5	1.1	0.4	1.5	1.0	0.4
γ	0.056		0.057	0.23	0.28	0.92	0.32	0.69	1.0	0.32	0.49	1.1	0.29	1.3	1.9

TABLE 4. Results of linear stability analysis. Wavelengths λ and exponential growth rates γ of the fastest growing modes are shown as functions of Ha and Gr.

where Π is the period of oscillations of a signal at a given point, and found that it varies little with Ha, Gr and λ and has the value close to the mean velocity value 1.0.

At the Hartmann numbers as high as 400 or 800, one usually expects near two-dimensionality of the flow, i.e. flow structures which are nearly uniform along

the magnetic field lines. As illustrated in figure 6(*d–f*), this is definitely true for our instability modes when the Hartmann number is high but the Grashof number is not very high so the transverse circulation in the base flow is either zero or weak. At lower *Ha* or higher *Gr* (see figure 6*a–c* and *g–i*), the instability modes are still strongly anisotropic with weak gradients along the magnetic field lines, but one can see significant deviation from two-dimensionality, which is apparently caused by the base flow circulation.

The values of *Gr* and *Ha* also affect the growth rate and streamwise wavelength of the most unstable mode. From table 4 and figure 5 we see two trends. One of them is that the increase of *Gr* leads to higher growth rate and shorter wavelength. The reason for the first part of this trend is evident. The second part can be explained by the transformation of the base flow. At higher *Gr*, the base flow has stronger transverse circulation and top–bottom asymmetry of streamwise velocity, both leading to a temperature distribution with unstable stratification more limited near the duct's bottom. This limits the vertical size of the most unstable modes and, since the rolls tend to have approximately equal streamwise and wall-normal dimensions, forces them to have a shorter wavelength.

The second trend that can be observed in table 4 and figure 5 is that increase of *Ha* causes higher growth rate γ. This is observed consistently with the only exception of the case $Gr = 10^7$ and *Ha* changing from 400 to 800. The trend is, at first glance, counterintuitive, since higher *Ha* generally means stronger suppression of flow by the Joule dissipation. In our case, however, the instability modes are either nearly uniform or vary weakly along the magnetic field lines. The Joule dissipation experienced by them is, therefore, weak and largely limited to the Hartmann boundary layers. At the same time, higher *Ha* means stronger suppression of the transverse circulation of the base flow, which, unlike the instability modes, has substantial velocity gradients along the magnetic field lines. As we have discussed in § 3, this leads to weaker mixing and more pronounced unstable stratification in the base flow. Our computations show that the resulting enhancement of instability potential is stronger than the reduction of this potential by the Hartmann friction of instability modes.

5. Direct numerical simulations

The computational domains and grids used for DNS are discussed in § 2.4 and summarized in table 2. The computational model is free from symmetry and periodicity constraints (except the inlet–exit periodicity on the scale of the flow domain), so three-dimensional nonlinear evolution of the flow is computed. Each simulation starts with the streamwise-independent base flow (see § 3) computed at the same *Ha* and *Gr*, to which random three-dimensional small-amplitude ($\sim 10^{-3}$) perturbations of velocity are added. The importance of consistent use of such initial conditions rather than the conditions in the form of a DNS flow obtained at another set of parameters stems from the fact that, as discussed later in this section, the base flow circulation remains a part of the DNS solution. Since the evolution of the circulation to its final state may take several thousands of time units (see § 3), and the DNS runs are, by necessity, shorter, the approach is needed to assure that a circulation of correct form is present in the flow. There remains a possibility that a different initial state would result in a different DNS solution (for example, with a different type of transverse circulation) at $t \to \infty$. A general analysis of this effect for our idealized system requires an unfeasibly large number of long DNS runs. In our view, such an analysis is also unnecessary. The uncertainty should be addressed

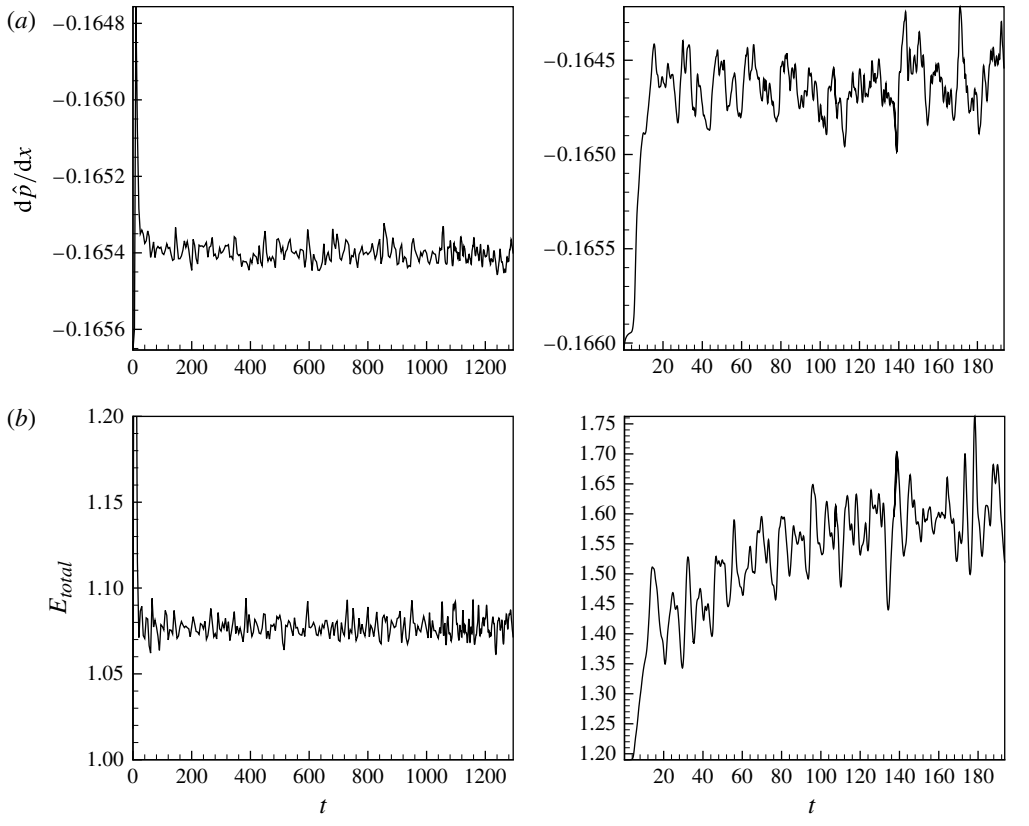

FIGURE 7. Time signals of the driving pressure gradient $d\hat{p}/dx$ (*a*) and the total kinetic energy of the flow (*b*) obtained in the DNS of flows at $Ha = 800$ and $Gr = 10^8$ (left column) and $Gr = 10^9$ (right column).

in future studies of more realistic systems, in particular, in studies of axially evolving flows with non-periodic inlet–exit conditions.

An illustration of the typical flow evolution during a DNS run is given in figure 7. We see that, after the instability and initial development, the flow reaches a fully developed state, in which the integral parameters fluctuate around steady means. The amplitudes of the fluctuations are small. The evolution of the fully developed flow is computed for at least 100 time units.

In all of our simulations, the velocity structure in fully developed flow has been found to include finite-amplitude roll-like structures (rolls in the following discussion) resulting from the instability, which are superimposed on a streamwise-independent mean flow. The convection rolls have irregular shapes and generate irregular time signals illustrated in figure 7. The flow fields have variations on the length scales in a wide range rather than just on the scale of the most dangerous instability mode. The absence of regularity is more pronounced at low *Ha*, although it is still the case at *Ha* as high as 800.

The flow is always anisotropic with the convection structures elongated in the direction of the magnetic field thus justifying their identification as rolls. The anisotropy becomes stronger at higher *Ha*. At the same time, as we illustrate below, realization of a quasi-two-dimensional form, with velocity and temperature being *y*-independent outside the Hartmann layers, is determined by both *Ha* and *Gr*.

The DNS solutions obtained in our computations can be classified into two general types. We will call them low-Gr and high-Gr flows with understanding that the boundary between 'low' and 'high' shifts with Ha. The criterion is the presence of significant streamwise-independent transverse circulation. In the low-Gr flows, the circulation is either absent in the base state (see figure 2*a*,*d*) or weak, so no noticeable traces of it remains in the DNS solution. This is observed at $Gr = 10^7$ when $Ha = 300$ and at $Gr = 10^7$ and 10^8 when $Ha = 400$ and 800. In the high-Gr flows, stronger convection effects result in base flows with strong transverse circulation, which persists in the DNS solutions. Such flows are found at $Gr = 10^7$, 10^8 and 10^9 when $Ha = 200$, $Gr = 10^8$ and 10^9 when $Ha = 300$, and $Gr = 10^9$ when $Ha = 400$ and 800.

The flow structures obtained in the DNS for low-Gr and high-Gr flows are illustrated on the example of two cases: $Ha = 800$, $Gr = 10^8$ and $Ha = 800$, $Gr = 10^9$. We start the discussion with the low-Gr case illustrated in figure 8. Distributions of vertical velocity u_z and temperature θ in the horizontal midplane $z = 0$ (see figure 8*a*,*b*) are nearly y-independent outside the Hartmann layers. Similar y-independency is found in other horizontal cross-sections, including those near the top and bottom walls, and in the two transverse cross-sections shown in figure 8(*c*). We conclude that quasi-two-dimensionality in the sense of Sommeria & Moreau (1982) is observed.

Figure 8(*a–c*) present a pattern of alternating upward and downward motions superimposed on the mean flow. The pattern is a manifestation of convection rolls, which are further illustrated by the streamwise vertical cross-sections $y = 0$ in figure 8(*d–f*). Distributions of vertical and streamwise velocity components u_z, u_x and temperature θ are shown. The spanwise velocity u_y is nearly zero in the flow. We see that the structure is quite irregular in this plane. The rolls have large amplitude, with u_z exceeding 0.5 of the mean streamwise velocity. This results in strong and irregular modulations of the streamwise velocity and temperature (see figure 8*d*,*e*). The flow completely loses its streamwise uniformity.

The typical structure of the high-Gr flow is illustrated by the case $Ha = 800$, $Gr = 10^9$ presented in figure 9. We first observe that quasi-two-dimensionality is incomplete in this case. The field of vertical velocity u_z is nearly two-dimensional outside the Hartmann layers (see figure 9*a*,*c*). At the same time, the temperature field in figure 9(*b*,*c*) shows strong variations in the y direction. An explanation is provided by the views of the flow structure in the transverse cross-sections given in figure 9(*c*). We see that the base flow circulation shown in figure 2(*e*) is retained by the DNS solution. The circulation's velocity is obscured by the strong convection roll-related motions in the core of the duct but can be clearly seen in the boundary layers near the top and bottom walls. The jet-like flow in these layers has the spanwise velocity u_y reaching the amplitude of approximately 0.25 of the mean streamwise velocity. This can be compared with the maximum $u_y = 0.126$ in the base flow itself.

The pattern of convection rolls (see figure 9*d–f*) is qualitatively similar to the pattern observed in the low-Gr case. The rolls are irregular. They are not located near the bottom wall, as one could expect on the basis of the linear stability analysis. Instead, the zones of strongest vertical velocity are distributed around the middle of the duct (see figure 9*d*). The amplitude of velocity in the rolls is high, with the maximum $|u_z|$ being nearly twice the mean streamwise velocity. This results in strong modulation of the distributions of the streamwise velocity u_x and temperature θ.

We note the similarity between the high-Gr regime illustrated in figure 9 and the regime found in the DNS of pipe flow at $Ha = 306$, $Gr = 8.298 \times 10^7$, $Re = 9046$ (all based on the pipe diameter) and $Pr = 0.022$ (see figure 14 of Zikanov *et al.* 2013). Specifically, in both the cases, the temperature and velocity fields are three-dimensional and dominated by convection rolls aligned with the magnetic field, but

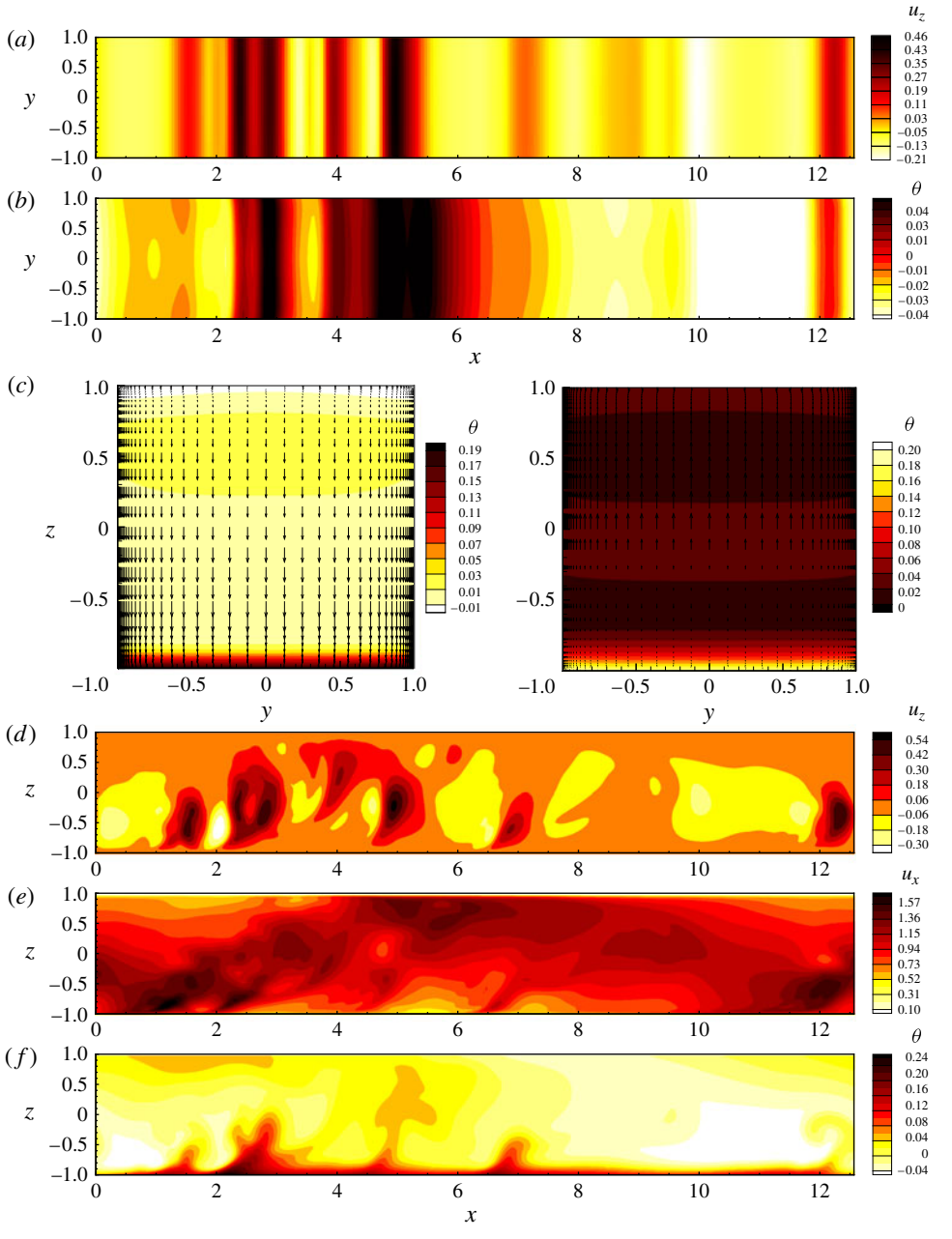

FIGURE 8. (Colour online) Flow structure at $Ha = 800$, $Gr = 10^8$ shown using instantaneous distributions of u_z (*a*) and θ (*b*) in the cross-section $z = 0$, of θ and velocity vectors in the cross-sections $x = 2\pi$ and $x = 4.0$ (*c*), and of u_z (*d*), u_x (*e*) and θ (*f*) in the cross-section $y = 0$.

retain features of the base flow circulation. It is possible that the low-*Gr* regime would be found in the pipe flow if DNS at higher *Ha* or lower *Gr* were conducted.

The perhaps most significant negative effect of the convection instability in the fusion reactor blankets is the resulting fluctuations of temperature at the walls.

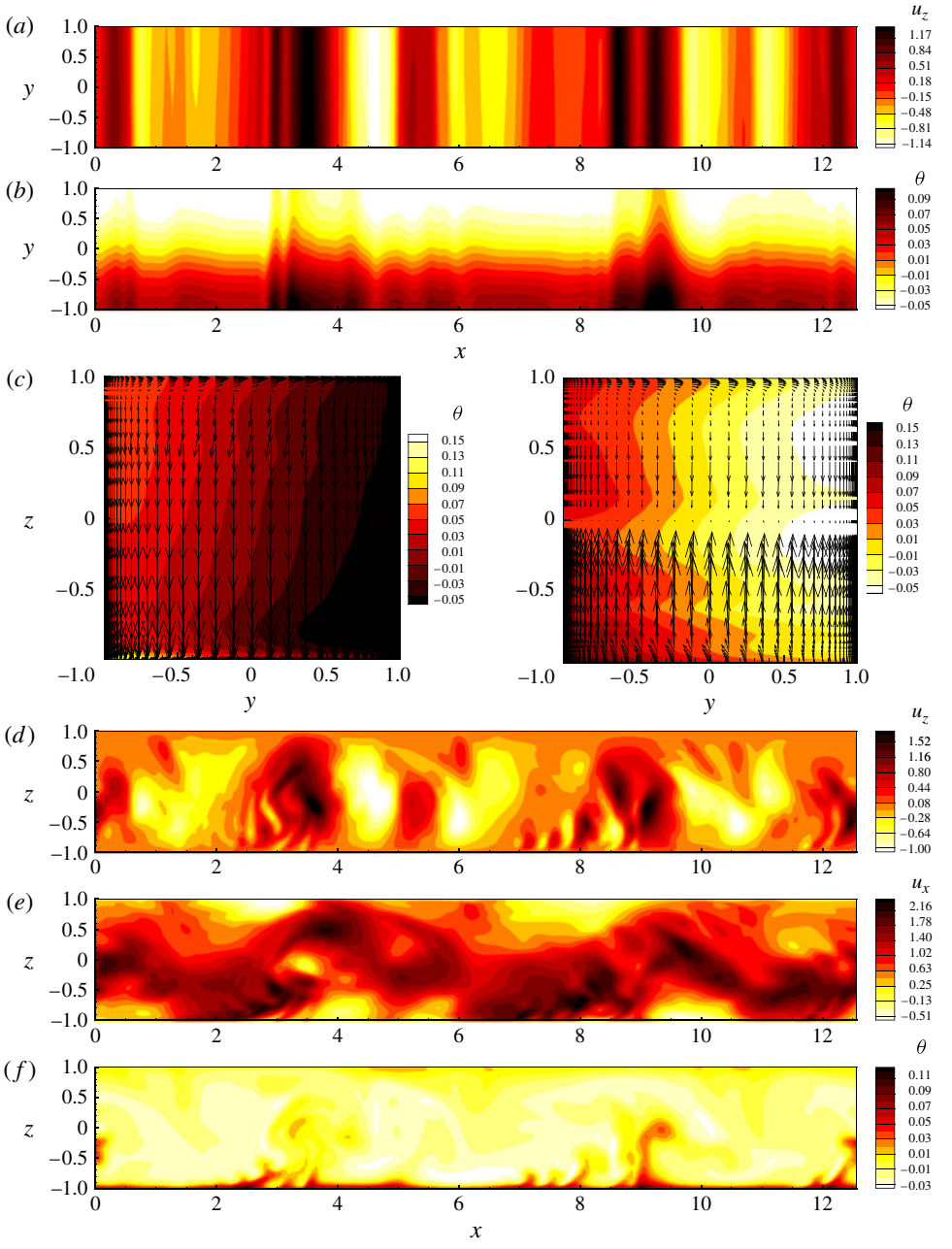

FIGURE 9. (Colour online) Flow structure at $Ha = 800$, $Gr = 10^9$ shown using instantaneous distributions of u_z (*a*) and θ (*b*) in the cross-section $z = 0$, of θ and velocity vectors in the cross-sections $x = 2\pi$ and $x = 8.0$ (*c*), and of u_z (*d*), u_x (*e*) and θ (*f*) in the cross-section $y = 0$.

If strong, the fluctuations would result in strong unsteady thermal stresses leading to rapid deterioration of wall material. In order to analyse this effect in our configuration, we have used the DNS solutions to record the temperature signals at several wall points during the stage of fully developed flow. The results are illustrated in figure 10.

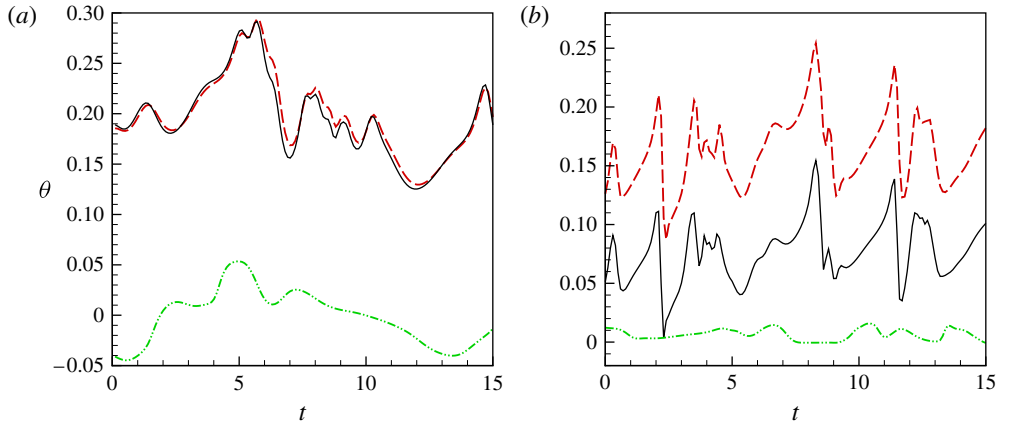

FIGURE 10. (Colour online) Time signals of temperature measured at the wall in fully developed flows at $Ha = 800$, $Gr = 10^8$ (*a*) and $Ha = 800$, $Gr = 10^9$ (*b*). The signals at $z = -1$, $y = 0$ (black, solid line), $z = -1$, $y = -0.95$ (red online, long-dash line), and $z = 1$, $y = 0$ (green online, dash-dot line) are shown.

We have found that the largest variations of temperature are observed at the heated bottom of the duct. The amplitude of the variations is quite high. In particular, at $Ha = 800$ and $Gr = 10^8$ and $Gr = 10^9$, it varies between 0.15 and 0.2 in terms of non-dimensional units. We can recalculate it into dimensional units by assuming the duct half-width $d = 5$ cm and using the physical properties of LiPb at 570 K (Mas de les Valls *et al.* 2008). This gives wall heat rate $q = 87$ W m^{-2} at $Gr = 10^8$ and $q = 870$ W m^{-2} at $Gr = 10^9$ (see (2.18)). Applying the temperature scale qd/κ, we find that the largest amplitude of fluctuations of wall temperature is in the range 5–6.6 K at $Gr = 10^8$ and in the range 50–66 K at $Gr = 10^9$. We can also estimate from figure 10 the typical time scale of the fluctuations as approximately 4 non-dimensional time units. At our parameters and for the hypothetical system just described, this gives approximately 10 s.

6. Concluding remarks

We have analysed mixed convection in a liquid metal flow in a duct with bottom heating and transverse magnetic field. The analysis extends much farther than previous analysis of the similar effects in the pipe flow by Zikanov *et al.* (2013). Most importantly, we consider a much broader range of Gr and Ha. The main conclusion is that the instability leading to the formation of convection rolls aligned with the magnetic field is a common feature of the flow invariably observed at $Ha \geqslant 200$ and sufficiently high Gr. The most dangerous modes of the instability have the form of rolls localized in the lower half of the duct and having the streamwise wavelength between, approximately, 1/4 and 1.0 of the duct width. The secondary flow regimes appearing as the result of the instability are irregular in space and time and involve a range of length scales, but retain the rolls aligned with the magnetic field as the most prominent feature of the velocity fields. The flows produce high-amplitude low-frequency temperature fluctuations.

It has been found in the DNS that the secondary flow regimes can be of one of the two types depending on whether Gr is smaller or larger than a certain

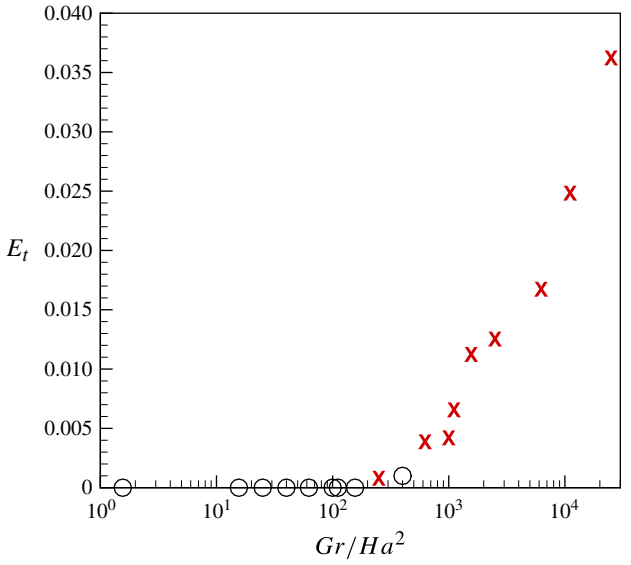

FIGURE 11. (Colour online) Kinetic energy of transverse circulation in the base flow E_t as a function of Gr/Ha^2. Circles and crosses indicate, respectively, the flows in which low-Gr and high-Gr regimes are observed in the DNS. Values of the parameter Gr/Ha^2 for each computed flow can be found in table 3.

threshold $Gr^*(Ha)$. The low-Gr type observed at $Gr < Gr^*$ is characterized by complete domination of the instability-generated spanwise rolls and by quasi-two-dimensional distributions of velocity and temperature. In the high-Gr flows at $Gr > Gr^*$, the spanwise rolls are combined with a streamwise roll similar to the circulation roll in the streamwise-uniform base flow. Significant flow and variations of temperature along the magnetic field lines are present.

The importance of the classification becomes clear when we consider that three-dimensional computations are unfeasible at the parameter values typical for a fusion reactor ($Ha \sim 10^4$ and Gr varying between 10^9 and 10^{12} depending on the location of the duct within the blanket and the type of the blanket). It is commonly assumed that the quasi-two-dimensional modelling in the spirit of Sommeria & Moreau (1982) can be utilized at high Ha (see the analysis of convection instabilities in vertical duct by Vetcha *et al.* (2013) as an example). Our results, however, demonstrate that even at high Ha the applicability of the model is not *a priori* certain. The model is applicable to the low-Gr regimes, but would be based on incorrect assumptions and produce erroneous results at the values of Gr, at which high-Gr regimes are realized.

We have no information about the structure of the flow at $Ha \sim 10^4$, $Gr \sim 10^9$–10^{12}. An attempt of extrapolation can be made, though. While analysing the results of our computations, we have noticed that the kinetic energy E_t of the transverse motion in the base flow (see table 3) can be accurately approximated as a function of the single parameter Gr/Ha^2, which represents the typical ratio between the buoyancy and Lorentz forces (see (2.7) and (2.8)). This can be seen in figure 11 and is confirmed by the regression analysis, which produces the coefficient of determination approximately 0.93. Assuming that the selection between low-Gr and high-Gr regimes is related to the strength of the circulation in the base flow and analysing the DNS data, we find that the threshold $Gr^*(Ha)/Ha^2$ is of the order of several hundreds. In the blanket

conditions, Gr/Ha^2 is between 10 and 10^4. We can, therefore, conclude that, for the specific system considered in our paper and as far as the suggested extrapolation to high Ha is correct (for which we have no proof at the moment), the flow at blanket conditions is likely to be of the low-Gr type at $Gr \leqslant 10^{10}$ and of the high-Gr type at higher Gr. Accordingly, the use of the quasi-two-dimensional model would be justified at $Gr \leqslant 10^{10}$ but not if the Grashof number is higher.

The results of our study are directly applicable only to the idealized system we have considered. Even if the idealized character is retained, the conclusions may change with the change of geometry. For example, no streamwise-oriented circulation rolls are expected in vertical ducts, so no analogies to our separation into low-Gr and high-Gr regimes is expected and the quasi-two-dimensional model may universally provide accurate results. In general, in order to fully understand the implications of our results for fusion reactor blankets, one has to consider specific designs with their complex geometry, inlet and exit effects, finite thermal and electrical conductivities of the walls, volumetric heating and the possibility of electromagnetic and thermal coupling between neighbouring ducts. Still, our study can be considered as a clear indication of the critically important role of convection in blanket's operation. As an example of a more direct relation, we may suggest the long poloidal ducts of the DCLL (dual coolant lithium-lead) blanket (Smolentsev *et al.* 2008). Some of the ducts are inclined at a significant (up to 30°) angle to the vertical. It is quite possible that convection-generated patterns similar to those found in our analysis would appear in these ducts.

Acknowledgements

Authors thank D. Krasnov for continuing assistance with the numerical model. Financial support was provided by the US NSF (grant CBET 1232851).

REFERENCES

ALBOUSSIÈRE, T., GARANDET, J. P. & MOREAU, R. 1993 Buoyancy-driven convection with a uniform magnetic field. Part 1. Asymptotic analysis. *J. Fluid Mech.* **253**, 545–563.

AUTHIÉ, G., TAGAWA, T. & MOREAU, R. 2003 Buoyant flow in long vertical enclosures in the presence of a strong horizontal magnetic field. Part 2. Finite enclosures. *Eur. J. Mech. (*B*/Fluids)* **22** (3), 203–220.

BRANOVER, H. 1978 *Magnetohydrodynamic Flow in Ducts*. Wiley.

DAVIDSON, P. A. 2001 *An Introduction to Magnetohydrodynamics*. Cambridge University Press.

GENIN, L. G., ZHILIN, V. G., IVOCHKIN, Y. P., RAZUVANOV, N. G., BELYAEV, I. A., LISTRATOV, Y. I. & SVIRIDOV, V. G. 2011 Temperature fluctuations in a heated horizontal tube affected by transverse magnetic field. In *Proceedings of the 8th International Pamir Conference on Fundamental and Applied MHD, Borgo, Corsica*, pp. 37–41.

KRASNOV, D., ZIKANOV, O. & BOECK, T. 2011 Comparative study of finite difference approaches to simulation of magnetohydrodynamic turbulence at low magnetic Reynolds number. *Comput. Fluids* **50**, 46–59.

KRASNOV, D. S., ZIKANOV, O. & BOECK, T. 2012 Numerical study of magnetohydrodynamic duct flow at high Reynolds and Hartmann numbers. *J. Fluid Mech.* **704**, 421–446.

LEE, D. & CHOI, H. 2001 Magnetohydrodynamic turbulent flow in a channel at low magnetic Reynolds number. *J. Fluid Mech.* **429**, 367–394.

LYUBIMOVA, T. P., LYUBIMOV, D. V., MOROZOV, V. A., SCURIDIN, R. V., HADID, H. B. & HENRY, D. 2009 Stability of convection in a horizontal channel subjected to a longitudinal temperature gradient. Part 1. Effect of aspect ratio and Prandtl number. *J. Fluid Mech.* **635**, 275–296.

MAS DE LES VALLS, E., BATET, L., DE MEDINA, V., FRADERA, J. & SEDANO, L. 2011 Qualification of MHD effects in dual-coolant DEMO blanket and approaches to their modelling. *Fusion Engng Des.* **86** (9–11), 2326–2329.

MAS DE LES VALLS, E., SEDANO, L., BATET, L., RICAPITO, I., AIELLO, A., GASTALDI, O. & GABRIEL, F. 2008 Lead–lithium eutectic material database for nuclear fusion technology. *J. Nucl. Mater.* **376** (3), 353–357.

MISTRANGELO, C. & BÜHLER, L. 2013 Magneto-convective flows in electrically and thermally coupled channels. *Fusion Engng Des.* **88** (9–10), 2323–2327.

MOLOKOV, S., MOREAU, R. & MOFFATT, H. K. 2007 *Magnetohydrodynamics: Historical Evolution and Trends*. Springer.

MORINISHI, Y., LUND, T. S., VASILYEV, O. V. & MOIN, P. 1998 Fully conservative higher order finite difference schemes for incompressible flow. *J. Comput. Phys.* **143**, 90–124.

NI, M.-J., MUNIPALLI, R., HUANG, P., MORLEY, N. B. & ABDOU, M. A. 2007 A current density conservative scheme for incompressible MHD flows at a low magnetic Reynolds number. Part I: On a rectangular collocated grid system. *J. Comput. Phys.* **227**, 174–204.

SMOLENTSEV, S., MOREAU, R. & ABDOU, M. 2008 Characterization of key magnetohydrodynamic phenomena for PbLi flows for the US DCLL blanket. *Fusion Engng Des.* **83**, 771–783.

SMOLENTSEV, S., MOREAU, R., BÜHLER, L. & MISTRANGELO, C. 2010 MHD thermofluid issues of liquid–metal blankets: phenomena and advances. *Fusion Engng Des.* **85** (7–9), 1196–1205.

SMOLENTSEV, S., MORLEY, M. & ABDOU, M. 2006 MHD and thermal issues of the SiCf/SiC flowchannel insert. *Fusion Sci. Technol.* **50**, 107–119.

SOMMERIA, J. & MOREAU, R. 1982 Why, how and when MHD-turbulence becomes two-dimensional. *J. Fluid Mech.* **118**, 507–518.

TAGAWA, T., AUTHIÉ, G. & MOREAU, R. 2002 Buoyant flow in long vertical enclosures in the presence of a strong horizontal magnetic field. Part 1. Fully-established flow. *Eur. J. Mech. (B/Fluids)* **21** (3), 383–398.

VETCHA, N., SMOLENTSEV, S., ABDOU, M. & MOREAU, R. 2013 Study of instabilities and quasi-two-dimensional turbulence in volumetrically heated magnetohydrodynamic flows in a vertical rectangular duct. *Phys. Fluids* **25** (2), 024102.

ZHAO, Y. & ZIKANOV, O. 2012 Instabilities and turbulence in magnetohydrodynamic flow in a toroidal duct prior to transition in Hartmann layers. *J. Fluid Mech.* **692**, 288–316.

ZIKANOV, O. 2010 *Essential Computational Fluid Dynamics*. Wiley.

ZIKANOV, O., LISTRATOV, Y. & SVIRIDOV, V. G. 2013 Natural convection in horizontal pipe flow with strong transverse magnetic field. *J. Fluid Mech.* **720**, 486–516.

ZIKANOV, O. & THESS, A. 1998 Direct numerical simulation of forced MHD turbulence at low magnetic Reynolds number. *J. Fluid Mech.* **358**, 299–333.